Strong Optical Field Ionization of Solids

Azza Ben Taher

Thesis submitted to the
Faculty of Graduate and Postdoctoral Studies
in partial fulfillment of the requirements for the degree of
MSc in Physics

Supervised by
Prof.Thomas Brabec

Ottawa Carleton Institute of Physics
Department of Physics
University of Ottawa
Ottawa, Canada

Abstract

Population transfer from the valence to conduction band in the presence of an intense laser field is explored theoretically in semiconductors and dielectrics. Experiments on intense laser driven dielectrics have revealed population transfer to the conduction band that differs from that seen in semiconductors. Our research explores two aspects of ionization in solids. (i) Current ionization theories neglect coupling between valence and conduction band and therewith the dynamic Stark shift. Our single-particle analysis identifies this as a potential reason for the different ionization behaviour. The dynamic Stark shift increases the bandgap with increasing laser intensities thus suppressing ionization to an extent where virtual population oscillation become dominant. The dynamic Stark shift plays a role dominantly in dielectrics which due to the large bandgap can be exposed to significantly higher laser intensities. (ii) In the presence of laser dressed virtual population of the conduction band, elastic collisions potentially transmute virtual into real population resulting in ionization. This process is explored in context of relaxation time approximation.

Keywords: Semiconductor; Dielectric; Stark Shift; Dephasing

Contents

Preface

First of all, I thank my God Almighty who stood up beside me to complete this science research praise him and thanks.

I would like to thank my professor Thomas Brabec for giving me the chance to join with his group to work on this exciting research, and for his helping and supporting me over the two years.

I am very grateful to Chris McDonald for his helping and advices to understand this research to be on the right way. Also special thank for all his help with cluster code and python program.

My husband gets special thanks, I do not think I could have completed my study here without his love and supporting me.

To my mother and my sibling for their love without this love I could not achieved my dreem to get my master degree.

Special lovely thanks to my beautiful daughter who is light of my life.

I would like to thank my country to give this opportunity to study abroad and its supporting me over the three years in Canada.

I am grateful to all my friends for their love and help to me, who are as my family here.

Finally, much of this work was published as C. R. McDonald, A. Ben Taher and T. Brabec, *Strong Optical Field Ionization in Solids*, J. Opt. **19**, 114005 (2017).

Chapter 1

Introduction

1.1 Ionization in atomic systems

In atomic systems, ionization is the process through which a bound electron is brought up into the continuum, becoming essentially a free electron. For over five decades, Keldysh theory [1] has been the generally accepted approach for understanding and interpreting the ionization that occurs when matter interacts with a strong laser field. In atomic systems Keldysh theory provides a simplified way of characterizing the ionization regime through the Keldysh parameter γ. For a laser field with a peak field strength of F_0 and an angular driving frequency of ω_0, the Keldysh parameter is given by,

$$\gamma = \frac{\omega_0}{eF_0}\sqrt{2m_eI_p} \tag{1.1}$$

where e and m_e are the charge and mass of the electron, respectively, and I_p is the ionization potential of the atom.

The figure (1.1) shows when the atomic system is exposed to the field of the laser, the combination of Coulomb potential and the effective potential of the laser pulse will cause the bound electron to feel a modified potential. Fig.(1.1(a)) shows when the field is weak enough that this modified potential felt by the electron differs only slightly from the Coulomb potential, the electron will need to absorb n-photons such that $n\omega_0 \geq I_p$ to be brought up into the continuum. This process is known as multiphoton ionization and occurs when $\gamma \gg 1$. Multiphoton ionization can be characterized by its scaling with the peak field strength. For an n-photon process, multiphoton ionization scales as F_0^{2n}. By contrast, in Fig.(1.1(b)) when the field is strong enough to cause a narrowing of the Coulomb barrier, the electron can escape by tunnelling through this reduced barrier. This process is known as tunnel ionization and occurs when $\gamma \ll 1$. Fig.(1.1(c)) shows a third, type of ionization can also occur. This happens when the field is so strong that the Coulomb barrier is bent down to such a degree that it lies below the ionization potential of the atom allowing the

electron to escape without tunnelling; this process is known as above-barrier ionization [2–4].

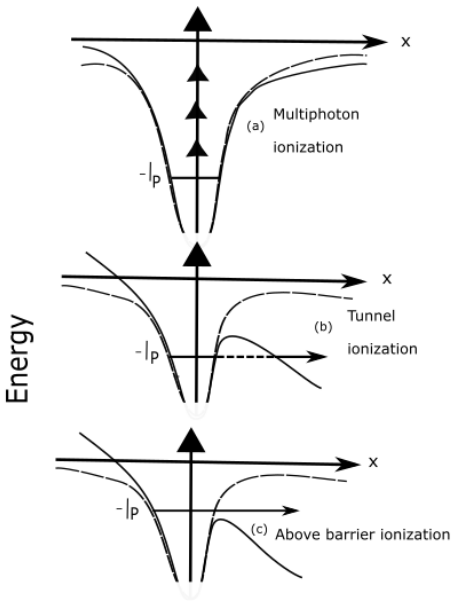

Figure 1.1: Ionization two different regimes. When the atomic system is exposed to the field laser the Coulomb potential will be changed. (a) is Multiphoton ionization regime. (b) is Tunnel ionization regime. (c) Above the barrier ionization.

1.2 Ionization in solids

In solid state systems ionization can be described as population originally residing in the valence band being brought up into the conduction band. These transitions result in the creation of electrons in the conduction band and holes in the valence band. As with atomic systems, Keldysh theory [1] has been the generally accepted approach for modelling the response of solids to intense underresonant laser fields. Recent experimental measurements of ionization in semiconductors [5] have proven to be consistent with Keldysh theory. These experiments show a conduction band population that increases in steps over each laser half cycle. By contrast, experiments on dielectrics [6–9] show a mainly oscillatory population exchange between valence and conduction band with little final conduction band population. These results indicate that the physical mechanisms driving ionization in dielectrics may differ from those in semiconductors and suggest the need to reexamine and amend Keldysh theory.

Currently a comprehensive understanding of the difference in physical processes driving the optical response and ionization of semiconductors and dielectrics is missing. In recent years, some progress has been made with gener-

alization of Keldysh theory, revealing some of its limitations [10–12]. Nevertheless, the physics responsible for the fundamental difference between ionization in semiconductors and dielectrics remains unresolved. As ionization is the first step in all strong field experiments, this deficiency impedes progress in wide range of topical areas. (i) Traditionally, intense laser solid interaction has played an important role in material machining [13] encompassing a wide field of applications ranging from medical surgery and bio-sensors [14] to state of the art material processing [15] , and to manufacturing of optical elements [16]; (ii) it was demonstrated that the oscillatory response of dielectrics to intense lasers can be exploited to optically modulate conductivity. This effect has opened enthralling perspectives for extending ultrafast electronics into the petahertz domain ($1\text{PHz} = 10^{15}\text{s}^{-1}$) [7, 8] and enabling petahertz signal processing [17]. (iii) Recent high harmonic generation experiments in dielectrics [9] and in semiconductors [18–24] have revealed ways to transfer attosecond technology from atomic to gases to solids. This has given birth to attosecond condensed matter physics.

Contemporary ionization theories take as a starting point the two-band semiconductor Bloch equations [25]. From here several approximations can be made to allow for a workable analytical model to be realized. The four most notable approximations used are:

(i) a semi-infinite bandgap [1],

(ii) the quasi-continuous wave approximation [1, 10, 12],

(iii) the frozen valence band approximation [1, 10–12],

(iv) and the neglect of many-body effects [1, 10–12].

Recent experimental evidence has demonstrated that the single-particle, two-band model provides a reasonable characterization of high-harmonic generation in semiconductor materials [23,24]. With this information in mind and given the complex nature of full many-body theory, it is reasonable for a first investigation to use single-particle approximations (i) - (iii) above and leave the examination of many-body effects for future work.

This thesis will consist of two main parts. In chapter 2 we examine ionization using the three different models: (i) the full two-band (2B) model where the dynamics in both valence and conduction band are considered. (ii) The frozen valence band (FVB) model where the dynamics of the valence band population are presumed to have an inconsequential effect on ionization. (iii) A generalized Keldysh (GK) model [26] where an arbitrary (periodic) band structure is introduced into the Keldysh framework. The generalized Keldysh model employs two approximations: (i) the FVB approximation and (ii) the quasi-continuous wave approximation. This allows for Keldysh theory to be applied to arbitrary bandgaps. Semiconductors and dielectrics are represented by a nearest-neighbour model. For the semiconductor we use a small minimum bandgap and wide bandwidth. By contrast, for the dielectric, we us a large minimum bandgap with a narrow bandwidth. Significantly contrasting physical

behaviours are observed in these two limits. The model semiconductor displays a physical behaviour that is consistent with the original Keldysh interpretation. Contrastingly, the dielectric displays an abundance of phenomena that reach beyond Keldysh theory; the origins of which can be identified by comparing the results from the different models.

First, ionization can be halted, in long pulses, when all of the integer photon channels become closed. In short pulses, where the pulse has a broad spectrum, non-integer photon channels can become the leading pathway by which population is transferred to the conduction band. Second, a potential mechanism that explains the unanticipated results seen in dielectric experiments [6–8] is identified. The bandgap of the material is widened as as result of the dynamic Stark shift. This, in turn, results in a suppression of ionization and predominantly affects materials with a larger bandgap because they can be subjected to fields with greater intensities. In models employing the FVB approximation, this effect is absent due to the absence of the dynamics in the valence band. In consequence of the suppressed ionization, the virtual population dynamics become the prominent observed behaviour.

In chapter 3, we will examine the effect that dephasing plays on ionization. This will be done within the context of the relaxation time approximation. We find that dephasing has a minor influence on optical field ionization itself; however, elastic collisions in the presence of (virtual) laser dressing can result in real population transfer to the conduction band. This comes as a result of the phase relation between polarization and laser being disrupted thus freezing part of the virtual population in the conduction band. The energy required for transforming virtual into real conduction band population is supplied by the laser field. This process is fundamentally different from laser assisted impact ionization which relies on inelastic collisions. Here we derive as simple analytical model and scaling law for material and laser parameters that can be used to experimentally corroborate or invalidate the relaxation time model.

In chapter 4 we will summarize our results and discuss possible future directions of research. As a final note, all equations below are given in atomic units unless otherwise stated.

Chapter 2

Regular optical field ionization in solids

In this chapter we will discuss the physics behind regular optical field ionization in a solid. To do this we will use a two-band model consisting of a single valence and a single conduction band. However, before ionization is discussed we will derive a set of equations of motion that describe the time dynamics of the solid interacting with an intense laser field. The derivation will be valid for an arbitrary number of bands but, for the purpose of our analysis, we will restrict ourselves to a two band system.

2.1 Equations of motion for a two-band system

We begin by expressing our wavefunction by the *ansatz*,

$$\Psi(\mathbf{x},t) = \sum_m \int_{BZ} a_m(\mathbf{k},t)\Phi_{m,\mathbf{k}}(\mathbf{x})d^3\mathbf{k} \tag{2.1}$$

where the $a_m(\mathbf{k},t)$ are the probability amplitudes of the wavefunction and the Φ_m's are the Bloch eigenstates for band m given by,

$$\Phi_{m,\mathbf{k}}(\mathbf{x}) = u_{m,\mathbf{k}}(\mathbf{x})e^{i\mathbf{k}\cdot\mathbf{x}} \tag{2.2}$$

with $u_{m,\mathbf{k}}$ being the periodic part of the Bloch function. The functions $\Phi_{m,\mathbf{k}}$ are eigenfunctions of the field-free Hamiltonian $H_0 = T + U$ with eigenvalues $E_{m,\mathbf{k}}$. Here T is the kinetic energy and U is the periodic potential of the lattice. All equations will be presented in atomic units; see Appendix A for conversions to SI units.

In the presence of the laser field $\mathbf{F}(t)$ the time-dependent Hamiltonian H is given by,

$$H(t) = H_0 - \mathbf{x}\cdot\mathbf{F}(t). \tag{2.3}$$

By substituting equation (2.1) into the time-dependent Schrödinger equation we obtain,

$$i\sum_m \frac{d}{dt}\int_{BZ} a_m(\mathbf{k},t)\Phi_{m,\mathbf{k}}(\mathbf{x})d^3\mathbf{k} = \big(H_0 - \mathbf{x}\cdot\mathbf{F}(t)\big)\int_{BZ} a_m(\mathbf{k},t)\Phi_{m,\mathbf{k}}(\mathbf{x})d^3\mathbf{k}. \tag{2.4}$$

By projecting $\Phi_{m,\mathbf{k}}$ into equation (2.4) we get,

$$i\dot{a}_m(\mathbf{k},t) = E_{m,\mathbf{k}}a_m(\mathbf{k},t) - \mathbf{F}(t)\cdot\sum_{m'}\langle\Phi_{m,\mathbf{k}}|\mathbf{x}|\Phi_{m',\mathbf{k}'}\rangle. \tag{2.5}$$

The term after the summation on the right hand side of equation (2.5) can be written as,

$$\begin{aligned}\langle\Phi_{m,\mathbf{k}}|\mathbf{x}|\Phi_{m',\mathbf{k}'}\rangle &= \int u^*_{m,\mathbf{k}}(\mathbf{x})e^{-i\mathbf{k}\cdot\mathbf{x}}\mathbf{x}u_{m',\mathbf{k}'}(\mathbf{x})e^{i\mathbf{k}'\cdot\mathbf{x}}d^3\mathbf{x}\\ &= i\int u^*_{m,\mathbf{k}}\bigtriangledown_{\mathbf{k}'}u_{m',\mathbf{k}'})e^{-i(\mathbf{k}-\mathbf{k}')\cdot\mathbf{x}}d^3\mathbf{x}\\ &\quad - i\int \Phi^*_{m,\mathbf{k}}\bigtriangledown_{\mathbf{k}'}\Phi_{m',\mathbf{k}'}d^3\mathbf{x},\end{aligned} \tag{2.6}$$

where the integral term on the right is,

$$\begin{aligned}i\int \Phi^*_{m,\mathbf{k}}\bigtriangledown_{\mathbf{k}'}\Phi_{m',\mathbf{k}'}d^3\mathbf{x} &= -i\bigtriangledown_{\mathbf{k}'}\langle\Phi_{m,\mathbf{k}}|\Phi_{m',\mathbf{k}'}\rangle\\ &= -i\bigtriangledown_{\mathbf{k}'}\delta_{m,m'}\delta_{\mathbf{k},\mathbf{k}'}.\end{aligned} \tag{2.7}$$

We notice here the integral on the left side can be written as,

$$\begin{aligned}i\int(u^*_{m,\mathbf{k}}\bigtriangledown_{\mathbf{k}'}u_{m,\mathbf{k}'})e^{-i(\mathbf{k}-\mathbf{k}')\cdot\mathbf{x}}d^3\mathbf{x} &= i\delta_{\mathbf{k},\mathbf{k}'}\int_X u^*_{m,\mathbf{k}}\bigtriangledown_{\mathbf{k}'}u_{m,\mathbf{k}'}d^3\mathbf{x}\\ &= \mathbf{d}_{mm'}(\mathbf{k})\delta_{\mathbf{k},\mathbf{k}'}.\end{aligned}$$

Where we have $|\mathbf{k}-\mathbf{k}'| \ll 1$, thus the integral for $e^{-i(\mathbf{k}-\mathbf{k}')\cdot\mathbf{x}}$ should give the Kronecker delta function $\delta_{\mathbf{k},\mathbf{k}'}$. For the other term we have the **transition dipole moment** which is,

$$\mathbf{d}_{mm'}(\mathbf{k}) = \int u^*_{m,\mathbf{k}}\bigtriangledown_{\mathbf{k}'}u_{m,\mathbf{k}'}d^3\mathbf{x} \tag{2.8}$$

where $\mathbf{d}_{mm'} = 0$ when $m = m'$. Finally we get the form of the dipole moment,

$$\langle\Phi_{m,\mathbf{k}}|\mathbf{x}|\Phi_{m',\mathbf{k}'}\rangle = -i\bigtriangledown_{\mathbf{k}'}\delta_{m,m'}\delta_{\mathbf{k},\mathbf{k}'} + \mathbf{d}_{mm'}(\mathbf{k})\delta_{\mathbf{k},\mathbf{k}'} \tag{2.9}$$

Therefore we can gain the probability amplitudes of the wavefunction by substituting equation (2.9), and the dipole moment is given (2.8) into (2.5),

$$\dot{a}_m(\mathbf{k},t) = (-iE_{m,\mathbf{k}} + F(t)\cdot\bigtriangledown_{\mathbf{k}})a_m(\mathbf{k},t) + i\sum_{m'\neq m}\Omega_{mm'}(\mathbf{k},t)a_{m'}(\mathbf{k},t) \tag{2.10}$$

where $\Omega_{mm'}(\mathbf{k},t) = F(t)\cdot\mathbf{d}_{mm'}(\mathbf{k})$.

To remove the term in equation (2.10) containing $\bigtriangledown_{\mathbf{k}}$ we make the transformation $\mathbf{k} = \mathbf{K} + A(t)$ where $A(t)$ is the vector potential defined by,

$$\frac{dA}{dt} = -F(t). \tag{2.11}$$

The Brillouin zone BZ is now shifted to the moving frame $\overline{\mathrm{BZ}} = \mathrm{BZ} - \mathbf{A}(t)$; in Appendix B the concept of the Brillouin zone and its relation to the reciprocal lattice is explained. Equation (2.10) now becomes,

$$\dot{a}_m(\mathbf{K},t) = -iE_m(\mathbf{K})a_m(\mathbf{K},t) + i\sum_{m'\neq m}\Omega_{mm'}(\mathbf{K},t)a_{m'}(\mathbf{K},t). \tag{2.12}$$

Making the transformation,

$$a_m(t) = b_m(t)e^{-i\int_{-\infty}^{t}[E_m(\mathbf{K}+\mathbf{A}(t'))dt']} \tag{2.13}$$

and putting it into equation (2.12) we get,

$$\dot{b}_m(\mathbf{K},t) = i\sum_{m'\neq m}\Omega_{mm'}(\mathbf{K},t)b_{m'}(\mathbf{K},t)e^{iS_{mm'}(\mathbf{K},t)} \tag{2.14}$$

where,

$$S_{mm'}(\mathbf{k},t) = \int_{-\infty}^{t}\varepsilon_{mm'}(\mathbf{K}+\mathbf{A}(t'))dt' \tag{2.15}$$

with $\varepsilon_{mm'} = E_m - E_{m'}$. When we restrict our solution to a single valence ($m = v$) and a single conduction ($m = c$) band we can write the band gap as $\varepsilon = E_c - E_v$ and $S_{mm'}$ becomes $S(\mathbf{K},t) = \int_{-\infty}^{t}\varepsilon(\mathbf{K}+\mathbf{A}(t'))dt'$. The equation of motion for $b_{v,c}$ are then,

$$\dot{b}_v(\mathbf{K},t) = i\Omega(\mathbf{K},t)b_c(\mathbf{K},t)e^{-iS(\mathbf{K},t)} \tag{2.16}$$

$$\dot{b}_c(\mathbf{K},t) = i\Omega^*(\mathbf{K},t)b_v(\mathbf{K},t)e^{iS(\mathbf{K},t)} \tag{2.17}$$

where $\Omega = \mathbf{F}\cdot\mathbf{d}$ and $\mathbf{d} = \mathbf{d}_{vc}$. For the numerical solution of the above differential equations, the fourth-order Runge-Kutta method is used; see Appendix C.

In the next section we will incorporate the finite bandgap into the Keldysh framework to derive a generalized version of Keldysh theory. This theory will then be compared with the results from equations (2.16) and (2.17).

2.2 The generalized Keldysh approach

We start from the full two-band (2B) equations (2.16) and (2.17) given above and use a vector potential of the form

$$\mathbf{A}(t) = -\hat{z}(F_0/\omega_0)f(t/\tau_0)\sin(\omega_0 t) \tag{2.18}$$

where, again, the electric field is given by $\mathbf{F}(t) = -d\mathbf{A}/dt$. Here F_0 is the peak field, ω_0 the circular frequency, $T_0 = 2\pi/w_0$ the oscillation period and f the pulse envelope with τ_0 the FWHM. We use the notation $\mathbf{k} = (k, \mathbf{k}_\perp)$ and $\mathbf{K} = (K, \mathbf{k}_\perp)$ with $k = K + A(t)$ and $\mathbf{k}_\perp$ crystal momenta parallel and perpendicular to laser polarization, respectively. The bandgap is expressed as,

$$\varepsilon(\mathbf{K}) = \overline{E}_{\mathrm{g}}(\mathbf{K}) + \varepsilon_{||}(k) \tag{2.19}$$

where E_{g} is the minimum bandgap and $\overline{E}_{\mathrm{g}} = E_{\mathrm{g}} + \varepsilon_\perp(\mathbf{K})$ with $\varepsilon_\perp$ being the general bandgap orthogonal to the laser polarization. Along the direction of laser polarization the bandgap is written as,

$$\varepsilon_{||}(k) = \sum_j^\infty \alpha_j \cos(jka) \tag{2.20}$$

where a is the lattice spacing which is related to the reciprocal lattice vector $k = 2\pi/a$ along the laser polarization direction. The bandwidth of the material is given by $\Delta = \max[\varepsilon_{||}]$.

Using the trigonometric identity $\cos(x+y) = \cos(x)\cos(y) - \sin(x)\sin(y)$, the bandgap $\varepsilon_\parallel\big(K + A(t)\big)$ can be written as,

$$\varepsilon_\parallel\big(K + A(t)\big) = \sum_j^\infty \alpha_j \Big\{ \cos(jKa)\cos\big(jaA(t)\big) - \sin(jKa)\sin\big(jaA(t)\big) \Big\}. \tag{2.21}$$

Making the Fourier-Bessel expansion, the trigonometric terms containing the vector potential above become,

$$\cos\big(jaA(t)\big) = J_0\big(j\beta f(t/\tau_0)\big) + 2\sum_{n=1}^\infty J_{2n}\big(j\beta f(t/\tau_0)\big)\cos(2n\omega_0 t) \tag{2.22}$$

$$\sin\big(jaA(t)\big) = 2\sum_{n=1}^\infty \Big\{ J_{2n-1}\big(j\beta f(t/\tau_0)\big)\sin\big((2n-1)\omega_0 t\big) \Big\}. \tag{2.23}$$

where the J_n's are the Bessel functions of the first-kind and $\beta = aF_0/\omega_0$ is the ratio of the Bloch frequency $\omega_b = aF_0$ to the angular frequency of the field. With this we can write the bandgap $\varepsilon = \varepsilon_{\mathrm{s}} + \varepsilon_{\mathrm{ns}}$ as the sum of the sinusoidal terms (ε_{s}) and the non-sinusoidal terms ($\varepsilon_{\mathrm{ns}}$); these are expressed as,

$$\varepsilon_{\mathrm{ns}}(\mathbf{K}, t) = \overline{E}_{\mathrm{g}}(\mathbf{K}) + \sum_{j=0}^\infty \Big\{ \alpha_j \cos(jKa) J_0\big(j\beta f(t/\tau_0)\big) \Big\} \tag{2.24}$$

$$\begin{aligned}\varepsilon_{\mathrm{s}}(\mathbf{K}, t) = {} & 2\sum_{j=0}^\infty \alpha_j \Big\{ \cos(jKa) \sum_{n=1}^\infty J_{2n}\big(j\beta f(t/\tau_0)\big)\cos(2n\omega_0 t) \Big\} \\ & - 2\sum_{j=0}^\infty \alpha_j \Big\{ \sin(jKa) \sum_{n=1}^\infty J_{2n-1}\big(j\beta f(t/\tau_0)\big)\sin\big((2n-1)\omega_0 t\big) \Big\}.\end{aligned} \tag{2.25}$$

This allows us to write the classical action as $S = S_{ns} + S_s$. With this, the equation (2.17) can be written as,

$$\dot{b}_c(\mathbf{K}, t) = iL(\mathbf{K}, t)e^{iS_{ns}(\mathbf{K},t)} \tag{2.26}$$

where,

$$L(\mathbf{K}, t) = \Omega^*(\mathbf{K}, t)b_{\mathrm{v}}(\mathbf{K}, t)e^{iS_s(\mathbf{K},t)}. \tag{2.27}$$

Expressed in terms of its Fourier transform, $L(K, t)$ is given as,

$$L(\mathbf{K}, t) = \frac{1}{\sqrt{2\pi}} \int_{-\infty}^{\infty} \tilde{L}(\mathbf{K}, \omega)e^{-i\omega t}d\omega. \tag{2.28}$$

In order to connect with Keldysh theory, we split $L(\mathbf{K}, t)$ into contributions from frequency bands of width σ yielding,

$$L(\mathbf{K}, t) = \sum_n L_n(\mathbf{K}, t)e^{-in\sigma t} \tag{2.29}$$

where,

$$L_n(\mathbf{K}, t) = \frac{1}{\sqrt{2\pi}} \int_{-\sigma/2}^{\sigma/2} \tilde{L}(\mathbf{K}, n\sigma + \omega)e^{-i\omega t}d\omega. \tag{2.30}$$

By replacing $\tilde{L}(\mathbf{K}, \omega)$ with its inverse Fourier transform, $L_n(\mathbf{K}, t)$ can further be expressed as,

$$L_n(\mathbf{K}, t) = \frac{\sigma}{2\pi} \int_{-\infty}^{\infty} dt' L(\mathbf{K}, t)e^{in\sigma t'} \mathrm{sinc}\Big(\frac{\sigma}{2\pi}(t - t')\Big) \tag{2.31}$$

where $\mathrm{sinc}(x) = \sin(\pi x)/(\pi x)$. Finally, we define the conduction band population through,

$$n_c(t) = \int_{\overline{BZ}} d^3K |b_c(\mathbf{K}, t)|^2 \tag{2.32}$$

which gives,

$$n_c(t) = \int_{\overline{BZ}} d^3K \Big| \sum_{n=-\infty}^{t} \int_{-\infty}^{t} dt' L_n(\mathbf{K}, t')R_n(\mathbf{K}, t') \Big|^2. \tag{2.33}$$

with R_n defined by,

$$R_n(\mathbf{K}, t) = e^{(iS_{\mathrm{ns}}(\mathbf{K},t) - in\sigma t)}. \tag{2.34}$$

The main virtue of the Keldysh type the equation (2.33) lies in providing a basis for analyzing ionization. The generalized Keldysh ionization theory is obtained by applying the following approximations to the equation (2.33).

Approximation 1 (frozen valence band) relies on setting $b_{\mathrm{v}}(\mathbf{K}, t) \approx b_{\mathrm{v}}(t = -\infty) = b_0$ in the equation (2.27); changes in the valence band are assumed to

have negligible influence on the transition dynamics from valence to conduction band [1, 27].

Approximation 2 (quasi-continuous wave) applies when the pulse envelope changes little over one oscillation period so that the envelope $f(t_s/\tau_0)$ in the equation (2.31) can be assumed constant; here t_s is a slowly varying time. By considering only the time-dependence of the rapidly varying sinusoidal functions and by choosing $\sigma = \omega_0$, the integral in the equation (2.31) becomes a Fourier series integral,

$$L_n(\mathbf{K}, t) = \frac{\omega_0}{2\pi} \int_{-T_0/2}^{T_0/2} dt' L(\mathbf{K}, t_s, t') e^{in\omega_0 t'}. \tag{2.35}$$

The time integral in the equation (2.33) can then be written as,

$$\int_{-\infty}^{t} L_n(\mathbf{K}, t') R_n(\mathbf{K}, t') dt' = L_n(\mathbf{K}, t_s) \int_{-\infty}^{t} R_n(\mathbf{K}, t') dt' \tag{2.36}$$

where the equation (2.33) then becomes,

$$n_c(t) = 2\pi t \int_{\overline{BZ}} d^3K \sum_{n=-\infty}^{\infty} \left\{ |L_n(\mathbf{K}, t_s)|^2 \delta(\varepsilon_{\rm ns}(\mathbf{K}, t_s) - n\omega_0) \right\}. \tag{2.37}$$

This gives non-zero results only for resonant n-photon channels satisfying energy conservation,

$$\overline{E}_g + \sum_{j=0}^{\infty} \alpha_j \cos(jKa) J_0(j\beta f(t_s/\tau_0)) - n\omega_0 = 0. \tag{2.38}$$

Equation (2.38) provides a condition for determining the crystal momenta at which the photon energy $n\omega_0$ is equal to the nonsinusoidal part of laser dressed bandgap $\varepsilon_{\rm ns}$. The Fourier coefficients L_n define the ionization dynamics of each channel, such as the different intensity scaling of ionization in the multiphoton and tunnelling regimes. Equation (2.38) is solved for $K = K_n(\beta, \mathbf{k}\perp, t_s)$. Since different n result in different K_n, products of $L_n^{'}s$ do not overlap in K-space and are zero when $n \neq n'$ in the equation (2.33). Real values of K_n represent an allowed energy conserving n-photon channel; that is the conduction band population displays net growth after the laser pulse has passed. The remaining channels with complex solutions are neglected in Keldysh theory. As these channels are not energy conserving, they contribute only to virtual population dynamics and will not result net growth of n_c after the laser pulse. The number of resonant channels and their dynamic evolution can substantially differ from Keldysh theory [10]; this difference will come from approximation 3, below. In the weak field limit, the number of available $n-$photon resonant channels is $n_r = \lfloor \triangle/\omega_0 \rfloor$. The lowest channel number $n1 = \lceil E_g/\omega_0 \rceil$, giving a set of integer number resonant channels $N_{\rm r} = \{n \in N | n_1 \leq n \leq n_1 + n_r - 1\}$. We note while the minimum $n-$photon channel is determined by the minimum

bandgap E_g, the bandwidth Δ determines the number of channels available for ionization. The number of resonant channels can be reduced by laser dressing of the bandgap. Depending on the argument of J_0, some or all of the K_n may turn complex. When this occurs these channels are closed to ionization and will contribute only to virtual population. The ionization from closing channels decays exponentially with $\propto \mathrm{Im}[K_n]$. In most cases this can be neglected, however, this is not necessarily the case when all channels are closed and a channel comes close to, but misses a reopening.

With the resonance condition in the equation (2.38), integration over the crystal momentum K longitudinal to the laser field in the equation (2.37) can be achieved. Using the δ-function condition, the ionization rate is given as,

$$\begin{aligned}\frac{dn_c}{dt_s} &= 2\pi \int_{\overline{BZ}} d^3K \sum_{n=-\infty}^{\infty} |L_n(\mathbf{K}, t_s)|^2 \frac{\delta(K - K_n)}{|\varepsilon'_{\mathrm{ns}}(\mathbf{K}_n, t_s)|} \\ &= 2\pi \int_{BZ\perp} d\mathbf{K}\perp \sum_{n\in N_r} \frac{|L_n(\mathbf{K}, t_s)|^2}{|\varepsilon'_{\mathrm{ns}}(\mathbf{K}_n, t_s)|} \end{aligned} \tag{2.39}$$

where $\mathbf{K} = (K, \mathbf{k}\perp)$, N_r is the set of all n-photon resonant channels, $\mathbf{BZ}\perp$ is the Brillouin zone orthogonal to laser polaraization, $\varepsilon'_{\mathrm{ns}} = d\varepsilon_{ns}/dK$ and $L_n(\mathbf{K}_n, t_s)$ can be written as,

$$\begin{aligned} L_n(\mathbf{K}_n, t_s) &= \frac{\omega_0}{2\pi} \int_{-\frac{T_0}{2}}^{\frac{T_0}{2}} dt' L_n(\mathbf{K}_n, t_s, t') e^{i\varepsilon_{\mathrm{ns}}(\mathbf{K}_n, t_s)t'} \\ &= \frac{\omega_0 b_0}{2\pi} \int_{-\frac{T_0}{2}}^{\frac{T_0}{2}} dt' \Omega^*(\mathbf{K}_n, t_s, t') e^{iS(\mathbf{K}_n, t_s, t')}. \end{aligned} \tag{2.40}$$

where the resonant condition in the equation (2.38) and $L(\mathbf{K}_n, t)$ in the equation (2.27) have been used when going from the first line to the second line in the equation(2.40). Note that the equation (2.39) applies to any bandgap and depends on time only through $f(t_s/\tau_0)$. Future, depletion is not contained in our GK calculations, but can be added by multiplying the right band side of the equation (2.39) with n_c [27].

Approximation 3 applies to the semi-infinite bandgap model used by Keldysh. In his original work, Keldysh used a bandgap of the form,

$$\varepsilon(k) = E_g \sqrt{1 + \frac{k^2}{m^* E_g}}, \tag{2.41}$$

where m^* is the reduced mass of the electron and hole [1]. Integration over the crystal momentum is extended to $\pm\infty$ leading to an infinite number of n-photon ionization channels. Here we use a finite bandgap which is essential to understand ionization in dielectrics.

2.3 Analysis of intense-field ionization in solids

The above models are used to study ionization in a 1D model semiconductor and a 1D dielectric with nearest neighbour band structure; where here we use $\alpha_0 = \alpha_1 = \Delta/2$ and $\alpha_j = 0$ for $j \geq 2$. For our model semiconductor we use a narrow bandgap and wide bandwidth. By contrast, our model dielectric has a wide bandgap with a narrow bandwidth. Our semiconductor has a bandgap of $E_g = 0.129$ a.u. and a band width of $\Delta = 0.6$ a.u. In addition, we use a lattice constant of $a = 5.32$ a.u. and a constant dipole momentum of $d = 3.46$ a.u. Our model dielectric is defined by the parameters $E_g = 0.33$ a.u.,$\Delta = 0.13$ a.u., $a = 9.45$ a.u. and $d = 5.66$ a.u. The materials are exposed to an intense laser field with a Gaussian envelope and angular frequency $\omega_0 = 0.06$ a.u. Results are obtained for both long and short pulses having widths $\tau_0 = 100T_0$ and $\tau_0 = 1.7T_0$, respectively. All the parameters that are chosen here based on experiments [5, 6].

In Fig.(2.1) the results of our calculations for the semiconductor are in the left column, the results for the dielectric are in the right. Figures (2.1)(a) and (c) show the final conduction band population in the semiconductor as a function of β using the 2B equations (2.16) and (2.17) (red), the FVB solution equation (2.17) with $b_v(t) = b_0$ (green), and GK equation (2.39) (blue) for a long (a) and a short (c) pulse, respectively. The overall agreement of all three approaches is good. Differences exist at large β where the valence band is emptied ($n_c \longrightarrow 1$). This is not surprising as depletion is not contained in either the FVB or GK calculations. Due to the quasi-continuous wave assumption, GK also underestimates short pulse ionization in the multi-photon limit where the Keldysh parameter (see caption) is $\gamma \gg 1$, see (2.1)(c). Due to the broad pulse spectrum, ionization can proceed via all frequency channels within the band and not just at $n\omega_0$. Thus, channels exist that are not accounted for by the GK theory. Figure (2.1)(e) shows the sub-cycle dynamics for $\beta = 1$ in (2.1)(c) for the 2B (red) and FVB (green) solutions. Here ionization proceeds stepwise at each half-cycle, as expected from conventional ionization theory, and in agreement with experiment [5].

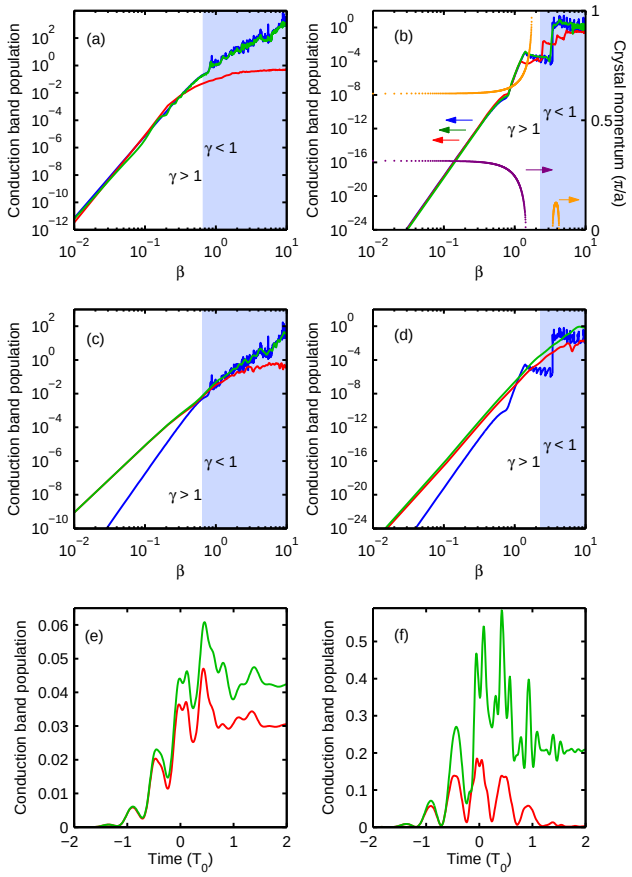

Figure 2.1: Left column: Ionization in a model semiconductor for a long (a) and short (c,e) pulse. Right column: ionization in a model dielectric for a long (b) and short (d,f) pulse. (a-d) The final conduction band population after the laser pulse versus $\beta = F_0 a/\omega_0$; the shaded region marks where the Kelydsh parameter $\gamma = (\omega_0/F_0 a)\sqrt{2E_g/\Delta} < 1$. (e) Time evolution for the short pulse in (c) at $\beta = 1$. (f) Time evolution for the short pulse in (d) at $\beta = 6.3$. The colors in (a-f) show the 2B solution (red), the FVB solution (green), and the GK solution (blue). Further, (b) shows the position of K_n for $n = 6$ (purple) and $n = 7$ (orange); the coloured arrows indicate the y-axis to which the line of corresponding colour belongs.

The right hand column of Fig.(2.1) shows the corresponding calculations for the dielectric. We first focus on the GK and FVB results in (2.1)(b)(long pulse) which agree well. The ionization characteristics for the dielectric (b) and semiconductor (a) for large β are markedly different. This difference is due, in large part, to the difference in material bandwidths. At $\beta = 0$, the semiconductor bandwidth has channels $N_r = \{3, ..., 12\}$, whereas, the dielectric has

$N_r = \{6, 7\}$. The small number of ionizing channels in the dielectric results in wide ranges of β for which all channels are closed. This is demonstrated by the purple ($n = 6$) and orange ($n = 7$) lines in Fig.(2.1)(b) which give K_n as a function of β; ionization terminates when there are no real K_n solutions. The large jump in ionization coincides with the re-opening and re-closing of channel $n = 7$ (see orange line). Comparison of original Keldysh and GK results for Fig.(2.1)(not shown here) shows good agreement everywhere except in dielectric where channel closing dominates the ionization dynamics. Termination of ionization can never happen in Keldysh theory, as a result of the semi-infinite bandgap model. For the large number of channels available to the semiconductor complete channel closing is unlikely. The 2B solution also reflects the physics as the FVB and GK solutions; however, the channel closing characteristics are altered.

Figure(2.1)(d) demonstrates the inadequacy of the GK approach for modelling the short pulse ionization dynamics in a dielectric. Here the FVB and 2B plots show similar behaviour with the 2B result being about two orders of magnitude lower than the FVB result at high field strengths. However, Fig. (2.1)(f) clearly shows that the FVB solution is inadequate to model the short pulse ionization dynamics in a dielectric. It depicts the time evolution of n_c for $\beta = 6.3$ in Fig (2.1)(d), which is close to highest intensity used in transient absorption spectroscopy experiments on SiO_2 [6]. The 2B solution shows mostly oscillations with very little final conduction band population, in agreement with experiment [6], whereas the FVB solution significantly overstates the expected level of ionization. The population oscillations arise from the non-resonant (virtual) terms in the equation (2.33). In what follows we will examine (i) how ionization occurs in dielectrics exposed to short pulses and (ii) what suppresses ionization in the 2B model.

When our dielectric is in the presence of the short pulses, it is exposed to a broad spectrum of frequencies. This permits ionization, not only at discrate $K_n^{'}s$, but over the whole Brillouin zone. To investigate what happens during ionization we use our expression for conduction band population in the equation(2.33) before the FVB approximatiom is made. The time dynamics of conduction band population is investigated for three frequency bands of width $\sigma\omega_0/2$ centred around $6\omega_0, 6.5\omega_0$ and $7\omega_0$; cross terms between these bands are negligible.

Figure(2.2)(a) shows the conduction band population dynamics for a low field strength where $\beta = 1.6$ and Fig.(2.2)(b) shows the population dynamics for a high field strength with $\beta = 6.3$; the dashed,dotted and solid lines represent the $6\omega_0, 6.5\omega_0$ and $7\omega_0$ channels respectively. For $\beta = 1.6$ in Fig. (2.2)(a) the $6\omega_0$ band is the largest contributor to the final conduction band population. This is surprising since the band containing the lowest order photon channel is expected to be the most efficient. However, there is also significant contribution from the $6.5\omega_0$ band. This is not included in the Keldysh theory. In Fig. (2.2) (b) where $\beta = 6.3$, the largest contributor to the final conduction band population comes from the $6.5\omega_0$ band. This occurs for a combination of two reasons.

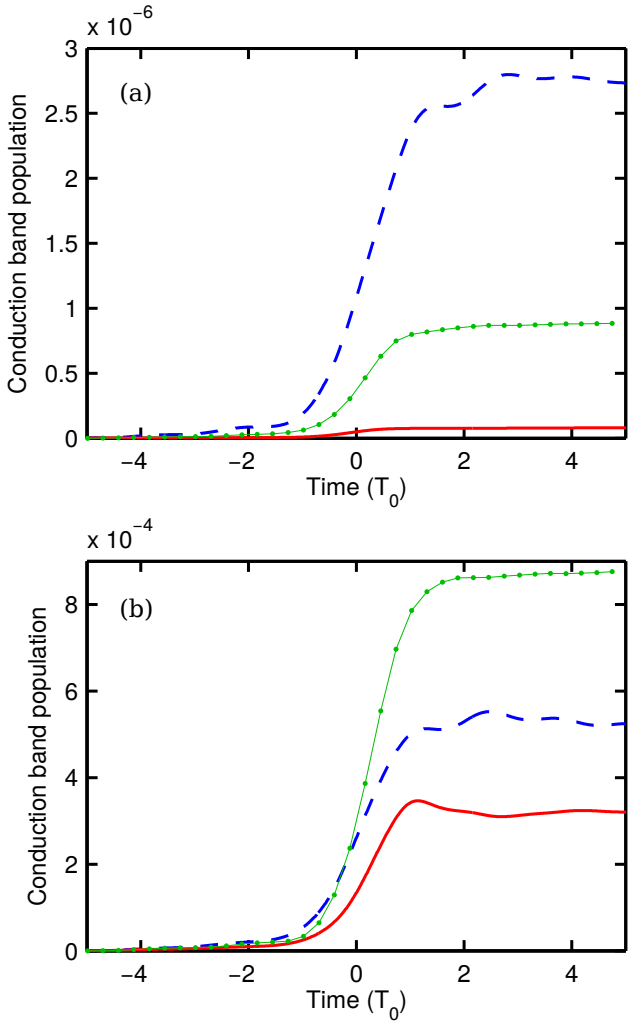

Figure 2.2: Short pulse time dynamics in the dielectric for the channels centred around $6\omega_0$ (dashed), $6.5\omega_0$ (dotted) and $7\omega_0$ (solid) for (a) $\beta = 1.6$ and (b) $\beta = 6.3$.

First, the growth of ionization in the $6\omega_0$ and $7\omega_0$ bands is impeded by the channel closings. Second, the $6.5\omega_0$ band contains frequencies around $\omega = E_g + \Delta/2 = 6.6\omega_0$ for which, for this particular band structure, there is always a solution to the resonance condition in the equation (2.38). As this frequency can be reached by the wide pulse spectrum, the $6.5\omega_0$ channel never closes and outgrows the others. The corresponding FVB calculations show similar physics-albeit with higher ionization-and hence are not shown here. We have repeated all dielectric calculations shown here for the SiO_2 parameters given in [9]. The

higher-order-cosine bandgap terms are weak and have little effect on the channel closings; the results remain unchanged.

The discussion above provided an answer to why the shape of the GK ionization curve in Fig.(2.1)(d) differs drastically from those from 2B and FVB curves. It does not, however, explain why the ionization in the 2B solution is significantly suppressed when compared to the FVB solution. The physics processes through which ionization occurs are the same for the 2B and FVB models. While the virtual population oscillations differ by approximately a factor of two, the final conduction band population differs by about two orders of magnitude (see Fig.(2.1)(f)). Since the suppression of ionization occurs when $n_c \ll 1$, depletion of the valence band cannot be the cause.

To determine the origin of the ionization suppression we must consider what is neglected when the FVB approximation is made. By making the FVB approximation, the coupling between valence and conduction band is neglected. When this coupling between bands is neglected, so is the dynamic shift which can lead to an increase in the energy difference to $\left(E_g^2+\Omega^2\right)^{1/2}$ [25,28] and ultimately result in less ionization. To test if this is ths case here, we will artificially manipulate the peak Rabi frequency $\Omega_r = dF_0$ by altering the transition dipole momentum d.

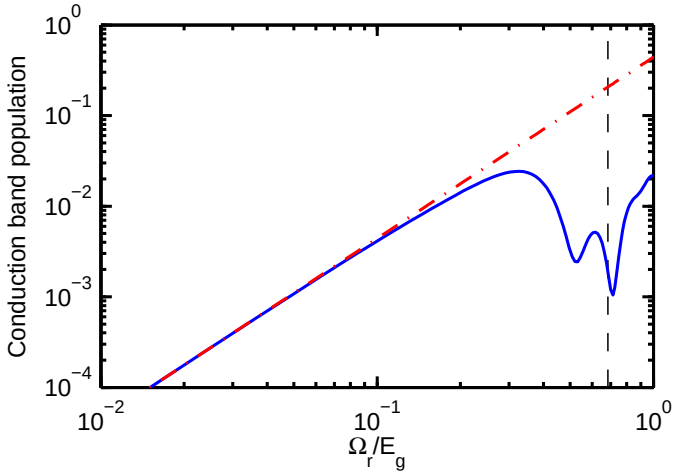

Figure 2.3: Final conduction band population for the dielectric in a short pulse as a function of Ω_r/E_g with $\beta = 6.3$ for the 2B (solid) and FVB solution (dash-dot); for all other parameters see Fig.2.1(e); Ω_r is changed by varying the dipole moment d. The dashed line indicates Ω_r/E_g used in Fig. 2.1(e).

In figure (2.3) the final conduction band population is plotted versus the ratio of peak Rabi frequency to the minimum bandgap. The dash dotted line represents solution from the FVB calculation and the solid line represents that from the 2B solution. When $\Omega_r/E_g \ll 1$ the two solutions agree. As the Rabi

frequency is increased the final conduction band population from the FVB solution grows monotonically with this increase in Rabi frequency. By contrast, the 2B solution displays significant suppression of ionization as the peak Rabi frequency starts to become comparable to the minimum bandgap energy. The same effect is also responsible for the differences in channel opening and closing and for the smaller jumps in the 2B solution in the long pulse limit in Fig.(2.1)(b). Finally, it is natural to ask why this behaviour is less relevant in the semiconductor. This can be answered by noting that the smaller bandgap limits exposure of the material to significantly weaker fields, thus rendering the dynamic Stark shift less pertinent.

Until now we have considered only a single wavelength; in what follows we briefly discuss the effect of increasing the driving field wavelength. To demonstrate the effect that a longer driving field wavelength will have on optical field ionization, we consider the generalized Keldysh model at two different values of ω_0 for dielectric.

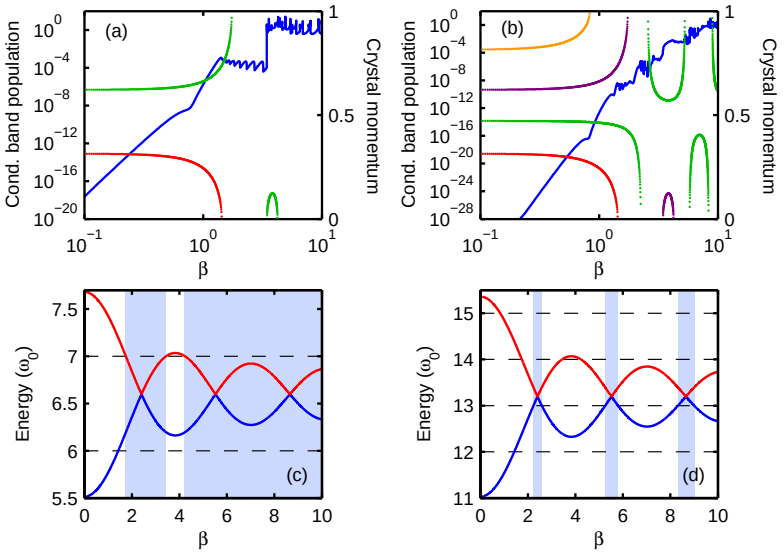

Figure 2.4: Top row: Final conduction band population calculated from the generalized Keldysh model (left y-axis) and the positions of the $K_n^{\prime}s$ (right y-axis) versus β for the dielectric for (a) $\omega_0 = 0.06$ a.u. with channels $n = 6$ (red) and $n = 7$ (green) and (b) $\omega_0 = 0.03$ a.u. with channels $n = 12$ (red), $n = 13$ (green), $n = 14$ (purple) and $n = 15$ (orange). Bottom row: Demonstration of channel closing for (c) $\omega_0 = 0.06$ a.u. and (d) $\omega_0 = 0.03$ a.u. The solid lines give the maximum (red) and minimum (blue) of the left hand side of Eq.(2.38). The dashed lines give the allowed n-photon transitions and the shaded regions indicate the range of β for which all channels are closed.

Figures(2.4)(a) and (2.4)(b) show the final conduction band population ver-

sus β calculated from the generalized Keldysh model(blue lines) for $\omega_0 = 0.06$ a.u. (same as Fig.(2.1)(b) and $\omega_0 = 0.03$ a.u.,respectively. When comparing the two curves, it is clear that the longer wavelength in Fig.(2.4)(b) has a behaviour much similar to that seen in the semiconductor. Also plotted in Figures (2.4)(a) and (2.4)(b) are the $K_n^{'}s$ (right y-axis) vs β. These curves in Fig.(2.4)(a) represent the $n = 6$ (red) and $n = 7$ (green) channels. Since the frequency used in Fig.(2.4)(b) is half that of (2.4)(a), there are twice as many channels available; these are $n = 12$ (red), $n = 13$ (green), $n = 14$ (purple) and $n = 15$ (orange). With the increase in available $n-$photon channels comes a decrease in ranges of β over which the equation (2.38) does not have a real solution. Figures (2.4)(c) and (2.4)(d) demonstrate the reason behind this behaviour. The solid lines indicate the maximum (red) and minimum (blue) of the first term in the equation (2.38) and the dashed lines give the $n-$photon resonances. When the dashed line is above the maximum or below the minimum that $n-$photon resonance channel is closed. As discussed above, conditions can arise where all $n-$photon channels are closed for a range of β. The ranges where all channels are closed are represented by the shaded regions. For $\omega_0 = 0.06$ a.u. there are only two possible channels; for $\omega_0 = 0.03$ a.u. there are twice as many. The increased density of channels within the bandwidth greatly reduces the range of β over which all $n-$photon resonance channels are closed; this complements what is show in the figures (2.4)(a) and (2.4)(b). The result is that the behaviour of the optical field ionization in dielectric approaches that seen in a semiconductor where many channels are supported.

This concludes our discussion of regular intense field ionization in solids. In the next chapter we will discuss effect of dephasing on ionization in the context of the relaxation time approximation.

Chapter 3

Effect of dephasing on intense-field ionization in solids

So far we have worked with the probability amplitude equations (2.16) and (2.17). However, in order to study the effect of dephasing on ionization it is beneficial to work with the density matrix equations as they allow for dephasing time to be included more naturally. Defining $n_m = |b_m|^2$ and $\pi = b_c^* b_v$ and combining these with the equations for $\dot{b}_{v,c}$ it is straightforward to obtain the density matrix equations for our two-band system; see Appendix D for more details.

$$\dot{n}_v(\mathbf{k}, t) = -i\Omega^*(\mathbf{K}, t)\pi(\mathbf{K}, t)e^{iS(\mathbf{K},t)} + \text{c.c.} \tag{3.1}$$

$$\dot{n}_c(\mathbf{k}, t) = i\Omega^*(\mathbf{K}, t)\pi(\mathbf{K}, t)e^{iS(\mathbf{K},t)} + \text{c.c.} \tag{3.2}$$

$$\dot{\pi}(\mathbf{K}, t) = -\frac{\pi(\mathbf{K}, t)}{T_2} - i\Omega(\mathbf{K}, t)w(\mathbf{K}, t)e^{-iS(\mathbf{K},t)} \tag{3.3}$$

where $w = n_v - n_c$. The first term on the hand right side of equation (3.3) is added as a phenomenological term to account for dephasing. This is known as the relaxation time approximation where T_2 is the dephasing or relaxation time.

3.1 Simple analytical model for the effect of dephasing on ionization

In this section we will derive an analytical expression for the conduction band population. We will do this by first using the frozen valence band approximation and then integrating over the crystal momentum. To simplify the derivation we will work in one dimension; however, the generalization to three dimensions is straightforward.

We begin by choosing the ansatz for $\pi(\mathbf{K}, t)$ as,

$$\pi(K,t) = g(K,t)e^{-t/T_2} \tag{3.4}$$

and substitute it into equation (3.3). This gives us the time derivative of $g(K,t)$ as,

$$\dot{g}(K,t) = -i\Omega(K,t)w(K,t)e^{-iS(K,t)}e^{t/T_2}. \tag{3.5}$$

This equation allows us to write $g(K,t)$ as the integral,

$$g(K,t) = -i\int_{-\infty}^{t} \Omega(K,t')w(K,t')e^{-iS(K,t')+t'/T^2}dt'. \tag{3.6}$$

We substitute equation (3.6) into equations (3.1) and (3.2) to get,

$$\dot{n}_v(K,t) = -\Omega^*(K,t)\int_{-\infty}^{t} dt'\Omega(K,t')w(K,t')e^{iS(K,t,t')-(t-t')/T_2} + \text{c.c.} \tag{3.7}$$

$$\dot{n}_c(K,t) = \Omega^*(K,t)\int_{-\infty}^{t} dt'\Omega(K,t')w(K,t')e^{iS(K,t,t')-(t-t')/T_2} + \text{c.c.} \tag{3.8}$$

where $S(K,t,t') = \int_{t'}^{t} \varepsilon_g[K + A(t'')]dt''$.

We now make the frozen valence band approximation where it is assumed that the valence band population changes very little over the laser pulse, ie. $n_v(K,t) \approx n_v(K,0)$. With this $\dot{n}_v(K,t) = 0$ and equation (3.2) becomes,

$$\dot{n}_c(K,t) = \Omega^*(k,t)\int_{-\infty}^{t} dt'\Omega(K,t')n_v(K,0)e^{iS(K,t,t')-(t-t')/T_2} + \text{c.c.} \tag{3.9}$$

Now the integral form of the conduction band population can be written as,

$$n_c(K,t) = n_v(K,0)\int_{-\infty}^{t} dt'\int_{-\infty}^{t'} dt''\Omega^*(K,t')\Omega(K,t'')e^{iS(K,t',t'')-(t'-t'')/T_2} + \text{c.c.} \tag{3.10}$$

where $n_v(K,0) = (2k_b)^{-1}$ with $k_b = \pi/a$.

3.1.1 Integration over the crystal momentum

Now we will integrate over the crystal momentum in equation (3.10). To do this we will use the nearest neighbour band gap [29],

$$\varepsilon(k) = E_g + \frac{\Delta}{2}(1 - \cos(ka)). \tag{3.11}$$

The bandgap appears in the exponent of equation (3.10) through $S(K,t',t'')$ as $\varepsilon_g(k + A(t))$. Using the trigonometric identity $\cos(x,y) = \cos(x)\cos(y) - \sin(x)\sin(y)$ we get,

$$\varepsilon_g(K+A(t)) = \left(E_g + \frac{\Delta}{2}\right) - \frac{\Delta}{2}\big(\cos aK\cos(aA(t)) - \sin aK\sin(aA(t))\big). \tag{3.12}$$

We substitute the equation (3.12) into the equation (3.10) then we obtain this expression,

$$n_c(K,t) = n_v(K,0)\int_{-\infty}^{t} dt'\Omega^*(t')\int_{-\infty}^{t'} dt''\Omega(t'')e^{-i(E_g+\frac{\Delta}{2})(t-t')} \times e^{-i\left(\cos aK\mathrm{Re}\{\phi\}-\sin aK\mathrm{Im}\{\phi\}\right)} + \text{c.c.} \tag{3.13}$$

where,

$$\phi(t',t) = \frac{\Delta}{2}\int_{t'}^{t} dt'' e^{iaA(t'')}. \tag{3.14}$$

We write the second exponent in equation (3.13) using Fourier-Bessel expansion to get,

$$\begin{aligned} e^{-i\left(\cos(aK)\mathrm{Re}\{\phi\}-\sin(aK)\mathrm{Im}\{\phi\}\right)} &= e^{-i\cos(aK)\mathrm{Re}\{\phi\}}e^{i\sin(aK)\mathrm{Im}\{\phi\}} \\ &= \sum_{n,m=-\infty}^{\infty}(-i)^n J_n(\mathrm{Re}\{\phi\})J_m(\mathrm{Im}\{\phi\})e^{i(m+n)aK}. \end{aligned} \tag{3.15}$$

All of the K-dependence is now contained in the $e^{i(m+n)aK}$ terms. Here we do the integration over K which will give,

$$\int_{-\frac{\pi}{a}}^{\frac{\pi}{a}} e^{i(m+n)aK}dK = \begin{cases} \frac{2\pi}{a} & \text{if } m+n=0 \\ 0 & \text{otherwise.} \end{cases} \tag{3.16}$$

Thus, the summation becomes,

$$\sum_{n,m=-\infty}^{\infty}(-i)^n J_n(\mathrm{Re}\{\phi\})J_m(\mathrm{Im}\{\phi\})\int_{-\frac{\pi}{a}}^{\frac{\pi}{a}} e^{i(m+n)aK}dK \tag{3.17}$$

$$\begin{aligned} &= \sum_{n=-\infty}^{\infty}(-i)^n J_n(\mathrm{Re}\{\phi\})J_{-n}(\mathrm{Im}\{\phi\})\left(\frac{2\pi}{a}\right) \\ &= \frac{2\pi}{a}\sum_{n=-\infty}^{\infty} J_n(\mathrm{Re}\{\phi\})J_n(\mathrm{Im}\{\phi\})\cos\left(\frac{n\pi}{2}\right) \\ &= \frac{2\pi}{a}J_0(\mathrm{Re}\{\phi\})J_0(\mathrm{Im}\{\phi\}) + \frac{4\pi}{a}\sum_{n=1}^{\infty} J_n(\mathrm{Re}\{\phi\})J_n(\mathrm{Im}\{\phi\})\cos\left(\frac{n\pi}{2}\right) \\ &= \frac{2\pi}{a}J_0(|\phi|). \end{aligned} \tag{3.18}$$

The final step results from summation theorem for Bessel Functions [30]. Finally, we obtain the conduction band population as function of the time,

$$n_c(t) = \int_{-\infty}^{t} dt'\Omega^*(t')\int_{-\infty}^{t'} dt''\Omega(t'')e^{[-i(E_g+\frac{\Delta}{2})(t'-t'')-1/T_2]}J_0(|\phi(t',t'')|) + \text{c.c.} \tag{3.19}$$

Note that all the information carried by the K-dependence is now carried by the J_0 term.

3.1.2 The inner integral over t''

The inner integral $\int_{-\infty}^{t'} dt''\Omega(t'')J_0(|\phi(t',t'')|)e^{(t''-t')/\alpha}$ where α is given by,

$$\alpha = \frac{T_2 + iT_2^2(E_g + \Delta/2)}{T_2^2(iE_g + \Delta/2)^2 + 1} \tag{3.20}$$

can be integrated by parts to give,

$$\begin{aligned}
&\int_{-\infty}^{t} dt''\Omega(t'')J_0(|\phi(t',t'')|)e^{(t''-t')/\alpha} \\
&= \alpha\Omega(t'')J_0(|\phi(t'',t')|)e^{(t''-t')/\alpha}\Big|_{-\infty}^{t'} \\
&\quad - \alpha\int_{-\infty}^{t'} dt''\left\{\dot{\Omega}(t'')J_0\big(|\phi(t'',t')|\big) - \Omega(t'')J_1\big(|\phi(t'',t')|\big)\frac{d}{dt''}|\phi(t'',t')|\right\}e^{(t''-t')/\alpha} \\
&= \alpha\Omega(t'') - \alpha^2\Big(\dot{\Omega}(t'')J_0(|\phi(t'',t')|) - \Omega(t'')J_1(|\phi(t'',t'))\frac{d}{dt''}|\phi(t'',t')|\Big)e^{(t''-t')}\Big|_{-\infty}^{t'} \\
&\quad + \alpha^2\int_{-\infty}^{t'} dt''\Big\{\ddot{\Omega}(t'')J_0\big(|\phi(t'',t')|\big) - 2\dot{\Omega}(t'')J_1\big(|\phi(t'',t')|\big)\frac{d}{dt''}|\phi(t'',t')| \\
&\qquad - \frac{1}{2}\Omega(t'')\Big[J_0|\big(|\phi(t'',t')|\big) - J_2\big(|\phi(t'',t')|\big)\Big(\frac{d}{dt''}|\phi(t'',t')|\Big)^2\Big] \\
&\qquad - \Omega(t'')J_1|\big(|\phi(t'',t')|\big)\frac{d^2}{dt''^2}|\phi(t'',t')|\Big\}e^{(t''-t')/\alpha} + \ldots
\end{aligned} \tag{3.21}$$

It is clear that the number of terms in the integral above quickly become overwhelming. To third order in α this integral is,

$$\begin{aligned}
\int_{-\infty}^{t} dt''\Omega(t'')J_0(|\phi(t',t'')|)e^{(t-t')/\alpha} = \alpha\Omega(t') - \alpha^2\dot{\Omega}(t') + \alpha^3\Big\{\ddot{\Omega}(t') \\
- \frac{1}{2}\Omega(t')\Big(\frac{d}{dt''}|\phi(t'',t')|\Big)^2\Big|_{t''=t'}\Big\} + ...
\end{aligned} \tag{3.22}$$

In order to obtain a simple expression expression for $n_c(t)$ we retain only the first two terms in equations (3.22) giving,

$$n_c(t) \approx \alpha\int_{-\infty}^{t}\big(|\Omega(t')|^2 - \alpha\Omega^*\dot{\Omega}(t')\big)dt' + \text{c.c.} \tag{3.23}$$

The equation(3.23) is similar to what would be obtained for a two-level system with energy gap of $E_g + \Delta/2$. For this the term $J_0\big(|\phi(t'',t')|\big)$ does not affect in the equation (3.23).

3.2 Analysis of dephasing on ionization

We start by solving the equations (3.2) and (3.3) for different values of T_2 for the semiconductor and dielectric. The materials are exposed to an intense laser pulse with angular frequency $\omega_0 = 0.057$ a.u. and width $\tau_0 = 10T_0$.

Figure (3.1) shows the conduction band population at the end of the laser pulse as a function of crystal momentum. The left column illustrates the results for the dielectric and the right column illustrates the results for the semiconductor. The top row has $T_2 = \infty$ (no dephasing); the dephasing time is shortened in the middle row and is further shortened for the bottom row (see figure caption for values of T_2) . In figures (3.1(a)) and (3.1(b)) where $T_2 = \infty$, the conduction band population only results from the regular optical field ionization.As T_2 is decreased the signature of the regular ionization is engulfed by population that develops throughout the entire Brillouin zone. The population grows out of the virtual ionization channels. As the phase between the electron and the laser field is destroyed by dephasing, the conduction band component of the virtual population is converted to real population and remains in the conduction band at the end of the pulse. Further, this process has less of an effect in the semiconductor because, here, the regular optical field ionization in the semiconductor is stronger than in the dielectric.

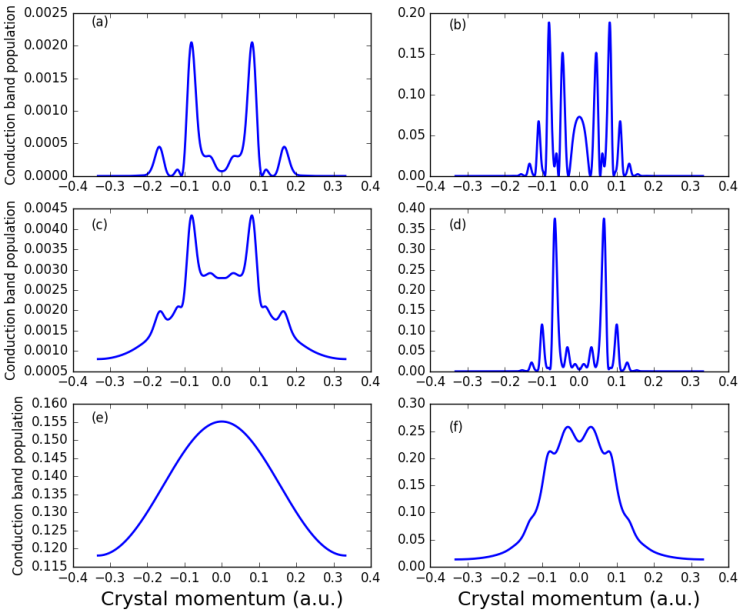

Figure 3.1: Final conduction band population vs crystal momentum for the dielectric (left column) at $F_0 = 0.01$ a.u. and the semiconductor (right column) at $F_0 = 0.008$ a.u. (a) Dielectric with $T_2 = \infty$. (b) Semiconductor with $T_2 = \infty$. (c) Dielectric with $T_2 = 100$ ps. (d) Semiconductor with $T_2 = 100$ ps. (e) Dielectric with $T_2 = 2$ fs. (f) Semiconductor with $T_2 = 2$ fs.

Figure (3.2) shows the time dynamics of the conduction band population for

the dielectric in a pulse of width $\tau_0 = 2T_0$ at $\omega_0 = 0.057$ a.u. and $F_0 = 0.01$ a.u. Figures (3.2(a)) and (3.2(b)) show a comparison between the solution of the equations (3.2), (3.3) (solid line) and the equation (3.23) (dashed line) for $T_2 = \infty$ and $T_2 = 10$fs, respectively. For these parameters, the equation (3.23) reproduces the conduction band population dynamics well. We expect that this agreement will not be as strong for the semiconductor (see Fig (3.1)) nor will it agree as well as the field strength is increased; this will become apparent in Fig.(3.3) below.

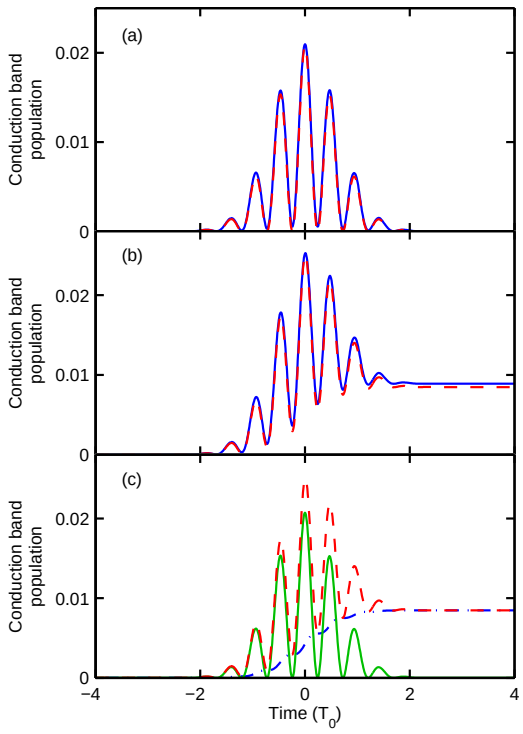

Figure 3.2: (a,b) Comparison of conduction band population dynamics for the dielectric exposed to a $\tau_0 = 2T_0$ pulse with field strength $F_0 = 0.01$ a.u. and angular frequency $\omega_0 = 0.057$ a.u. as calculated by Eqs.(3.2), (3.3) (solid,blue) and Eq. (3.23) (dashed,red); (a) $T_2 = \infty$ and (b) $T_2 = 10$ fs. (c) Contributions of the first (dash-dot, blue) and second (solid, green) terms under the integral in Eq. (3.23) to the conduction band population dynamics for $T_2 = 10$ fs; the dashed line (red) is the sum of the other two terms and is the same as dashed line in (b).

Figure (3.2(c)) demonstrates how each term in the integral of the equasion (3.23) contributes to the conduction band population dynamics for the parameters used in Fig.(3.2(b)). The dash-dot (blue) line shows the contribution from the first term. This term provides an increase in conduction band population

over each half-cycle; this population remains in the conduction band at the end of pulse. The solid (green) line shows the contribution of the second term. Here the conduction band population oscillates with a frequency twice that of the driving field and does not provide any contribution to the final conduction band population.In this light, the first term describes the ionization dynamics and the second term gives the virtual population dynamics.

With the understanding that the first term under the integral in the equation (3.23) is responsible for ionization, we can deduce an approximate scaling law for the final conduction band population in term of T_2 and F_0; that is,

$$n_c(t_{end}) \propto F_0^2 \frac{2T_2}{T_2^2(E_g + \Delta/2)^2 + 1} \tag{3.24}$$

The F_0^2 scaling in the expression above is consistent with numerical calculations of Zhokhov [11].

Figure (3.3(a)) compares the final conduction band population from the equations (3.2) and (3.3) in a 10 cycle field with $\omega_0 = 0.057$ for the dielectric with behaviour predicted by Eq.(3.23) (dashed lines) for different field strengths; the field strengths are at $F_0 = 0.001$ a.u. (circles), $F_0 = 0.005$ a.u. (squares) and $F_0 = 0.01$ a.u.(triangles). Figure (3.3(b)) shows similar calculations for the semiconductor at $F_0 = 0.001$ a.u. (circles), $F_0 = 0.005$ a.u. (square) and $F_0 = 0.008$ a.u. (triangles). For both materials the population scales as $T_2(T_2^2(E_g + \Delta/2)^2 + 1)^{-1}$ over the range of T_2's for the low field strength. As the field strength is increased, the scaling is only matched at the shortest T_2's where dephasing is strongest.

Figure (3.3(c)) shows the final conduction band population from the equasions (3.2) and (3.3) versus F_0 for the dielectric at $T_2 = \infty$ (circles), $T_2 = 10$ ps (squares) and $T_2 = 100$ fs (triangles). The dashed lines show the F_0^2 scaling predicted multiphoton scaling. At $T_2 = \infty$ the regular optical field ionization takes place. As T_2 is decreased to 10 ps, the low field ionization begins to scale as F_0^2, eventually beginning to transition to the regular optical field ionization behaviour as the field strength increases.

For the shorter time of 100 fs the ionization behaviour breaks from the F_0^2 scaling at high field strengths but does not recover the usual optical field ionization behaviour up to the strongest field strength plotted. Figure (3.3(d)) displays similar calculations to those in (c) for the semiconductor at $T_2 = \infty$ (circles), $T_2 = 10$ ps (triangles) and $T_2 = 100$ fs (squares). As with the dielectric,the F_0^2 scaling that transitions into the usual ionization behaviour at high fields is observed. However, since the regular optical field ionization is stronger in semiconductor, even the 100 fs result transitions to this behaviour at high field strengths.

The ionization behaviour shown in figures (3.3(c)) and (3.3(d)) provide a way to experimentally validate the predication of the ionization behaviour within the relaxation time approximation.

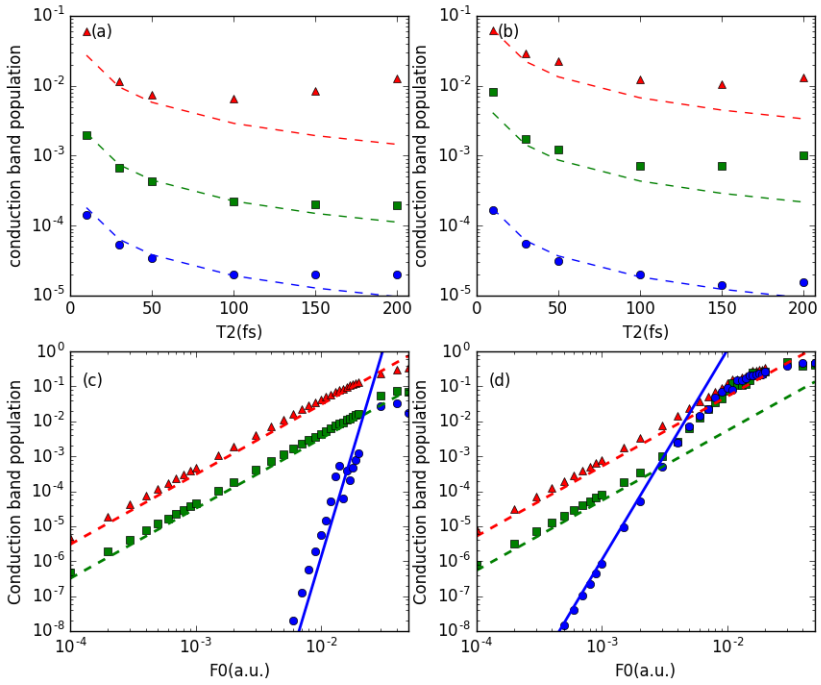

Figure 3.3: (a) Final conduction band population vs T_2 for dielectric with $F_0 = 0.001$ a.u. (circles), $F_0 = 0.005$ a.u. (squares) and $F_0 = 0.01$ a.u. (triangles). The dashed lines show the expected scaling behaviour for Eq.(3.24). (b) corresponding calculations from (a) for the semiconductor with $F_0 = 0.001$ a.u. (circles), $F_0 = 0.005$ a.u. (squares) and $F_0 = 0.008$ a.u. (triangles). (c) Final conduction band population vs peak field strength for $T_2 = \infty$ (circles) , 10 ps (squares) and 100 fs (triangles) in the dielectric. (d) Final conduction band population vs peak field strength for $T_2 = \infty$ (circles), 10 ps (squares) and 100 fs (triangles) in the semiconductor. In (c) and (d) the dashed lines show the expected scaling behaviour for Eq. (3.24) and the solid lines demonstrate the expected multiphoton scaling from regular optical field ionization.

Chapter 4

Conclusion

In conclusion, the regular optical field ionization of dielectrics in near-IR lasers was found to be strongly influenced by channel closing and dynamic Stark effect. These effects depend strongly on pulse shape and parameters, thus opening the potential for coherent control of optical field ionization in dielectrics. At longer wavelenghts, channel closing will be less important due to the increase in the number of resonant photon channels. As a result, in the mid-IR and longer wavelength regimes optical field ionization in dielectrics is expected to resemble that of semiconductors. While these physical processes will be similar, in our model optical field ionization remains suppressed due to the dynamic Stark shift which is independent of wavelength. In a more complete model, laser heating and impact ionization will lower the material damage intensity. Particularly in long pulses, damage might occur before intensities are reached at which the dynamic Stark shift becomes relevent. Electron quiver velocity scales as F_0/ω_0; for longer wavelengths the quiver velocity increases and, therefore, during collisions more energy is transferred from the laser to the electrons. The increased energy results in an increase of impact ionization.

In addition to the regular field ionization and impact ionization, the relaxation time approximation predicts that real population transfer to the conduction band can also occur as a result of dephasing. This population transfer results from a loss in the phase relation between electron and field due to elastic collisions. In the low field regime, the final conduction band population is expected to scale as F_0^2 providing a signature for experimental validation. We note, however, that the relaxation time approximation may be an oversimplified model for the laser-matter interactions studied here and likely overestimates the amount of ionization. A more complete model would build on a quantum statistical analysis, in which the two band equations are coupled to a phonon heat bath.

Finally, in a more complete description many-body effects will need to be investigated. For example, electron-hole interaction modifies the bandgap and introduces internal dipole fields that modify the Rabi frequency [25], thus potentially further influencing ionization.

Appendix A

Conversion between SI and atomic units

In the atomic units system, units of energy are given by the Hartree energy,

$$E_h = \frac{me^4}{(4\pi\epsilon_0\hbar)^2} \tag{A.1}$$

where m is the free-electron mass, e is the electron charge and ϵ_0 is the vacuum permittivity. Further, units of length are given by the Bohr radius,

$$a_0 = \frac{4\pi\epsilon_0\hbar^2}{me^2} \tag{A.2}$$

and units of time given by $\hbar/E_h$. The list below gives the conversions between atomic and SI units:

(i) Electric Field Strength: 1 au = 5.1422×10^{11} V/m

(ii) Mass: 1 au = 9.109×10^{-31} kg

(iii) Charge: 1 au = 1.602×10^{-19} C

(iv) Time: 1 au = 2.4189×10^{-17} s

(v) Energy: 1 au = 4.3597×10^{-18} J

(vi) Electric Potential: 1 au = 27.211 V

(vii) Length: 1 au = 0.52918×10^{-8} cm

Appendix B

Description of the Brillouin zone

B.1 The Bravais lattice

A crystal structure is composed of a periodic array of units. The concept of a *Bravais lattice* determines how these units are arranged. The three-dimensional Bravais lattice consists of all points with position vectors of the form,

$$\mathbf{R} = n_1\mathbf{a}_1 + n_2\mathbf{a}_2 + n_3\mathbf{a}_3 \tag{B.1}$$

where the $\mathbf{a}_i$'s, $i = 1, 2, 3$, are any three vectors not all belonging to the same plane; these are know as *primitive vectors*. The n_i's range through all integral values; thus, the point $n_i\mathbf{a}_i$ can be reached by moving n_i units along direction $\mathbf{a}_i$.

The *primitive unit cell* of a crystal lattice is a volume of space that, when translated through all vectors in the Bravais lattice, just fill all of the space without overlapping or leaving any voids. For a given Bravais lattice there is no unique choice of primitive unit cell; however, the *Wigner-Seitz* cell gives a primitive cell that possesses the full symmetry of the Bravais lattice. The Wigner-Seitz cell about a lattice point is defined as the region of space that is closer to that lattice point than any other lattice point [31].

B.2 The reciprocal lattice

The *reciprocal lattice* is defined as the set of all wavevectors $\mathbf{K}$ that give the periodicity of a given Bravais lattice. That is, $\mathbf{K}$ belongs to the reciprocal lattice of a Bravais lattice $\mathbf{R}$ if,

$$e^{i\mathbf{K}\cdot\mathbf{R}} = 1 \tag{B.2}$$

for all $\mathbf{R}$ in the Bravais lattice.

The reciprocal lattice is itself a Bravais lattice characterized by the primitive vectors $\mathbf{b}_i$ where $i = 1,\, 2\, 3$ and

$$\mathbf{b}_i \cdot \mathbf{a}_j = 2\pi\delta_{ij} \tag{B.3}$$

with δ_{ij} being the Kronecker delta function. Any $\mathbf{K}$ can be written a linear combination of the $\mathbf{b}_i$ as,

$$\mathbf{K} = k_1\mathbf{b}_1 + k_2\mathbf{b}_2 + k_3\mathbf{b}_3 \tag{B.4}$$

where k_i are integer valued. The *first Brillouin zone* is defined as the Wigner-Seitz cell of the reciprocal lattice. In the case of a cubic crystal with lattice constants a_i, the first Brillouin zone along each direction is given by $2\pi/a_i$.

Appendix C

Numerical solution of the two-band equations

This appendix illustrates how we get the numerical solution for the two-band probability amplitude equations,

$$\dot{b}_v(\mathbf{K},t) = i\Omega(\mathbf{K},t)b_c(\mathbf{K},t)e^{-iS(\mathbf{K},t)} \tag{C.1}$$

$$\dot{b}_c(\mathbf{K},t) = i\Omega^*(\mathbf{K},t)b_v(\mathbf{K},t)e^{iS(\mathbf{K},t)}, \tag{C.2}$$

where each term is as defined in the main text. We begin by defining,

$$\Phi(\mathbf{K},t) = e^{i\int_{-\infty}^{t}\varepsilon(\mathbf{K},t)dt'} \tag{C.3}$$

Inserting equation (C.3) into the differential equations above, we get the system of equations,

$$\dot{b}_v(\mathbf{K},t) = i\Omega(\mathbf{K},t)b_c(\mathbf{K},t)\Phi^*(\mathbf{K},t) \tag{C.4}$$

$$\dot{b}_c(\mathbf{K},t) = i\Omega^*(\mathbf{K},t)b_v(\mathbf{K},t)\Phi(\mathbf{K},t) \tag{C.5}$$

$$\dot{\Phi}(\mathbf{K},t) = i\varepsilon(\mathbf{K})\Phi(\mathbf{K},t) \tag{C.6}$$

To solve these equations numerically, we use the **fourth-order Runge-Kutta method** [32,33]. This method is an explicit method for solving ordinary differential equations of the form,

$$\dot{y} = f(t,y), \tag{C.7}$$

subject to the initial condition $y(t_0) = y_0$. At each time step the solution is advanced according to,

$$y_{n+1} = y_n + \frac{h}{6}(k_1 + 2k_2 + 2k_3 + k_4) \tag{C.8}$$

$$t_{n+1} = t_n + h \tag{C.9}$$

where,

$$k_1 = f(t_n, y_n), \tag{C.10}$$

$$k_2 = f(t_n + \frac{h}{2}, y_n + \frac{h}{2}k_1), \tag{C.11}$$

$$k_3 = f(t_n + \frac{h}{2}, y_n + \frac{h}{2}k_2), \tag{C.12}$$

$$k_4 = f(t_n + h, y_n + hk_3). \tag{C.13}$$

In our calculations, the initial condition is given as,

$$b_v(\mathbf{K}, 0) = \frac{1}{\sqrt{2k_b}} \tag{C.14}$$

$$b_v(\mathbf{K}, 0) = 0 \tag{C.15}$$

$$\Phi(\mathbf{K}, 0) = 0 \tag{C.16}$$

where $k_b = 2\pi/a$ is the reciprocal lattice vector and a is the lattice spacing. Our calculations are done using 600 k-space points in the first Brillouin zone.

Appendix D

Obtaining the density matrix equations from the probability amplitude equations

To work with the density matrix equations we define $n_m = |b_m|^2$ and $\pi = b_c^* b_v$. Here we show how to go from the probability amplitude equations to the density matrix equations. We begin with the equations for $\dot{b}_v$ and $\dot{b}_c$ which are,

$$\dot{b}_v(\mathbf{K},t) = i\Omega(\mathbf{K},t) b_c(\mathbf{K},t) e^{-iS(\mathbf{K},t)} \tag{D.1}$$

$$\dot{b}_c(\mathbf{K},t) = i\Omega^*(\mathbf{K},t) b_v(\mathbf{K},t) e^{iS(\mathbf{K},t)} \tag{D.2}$$

where all terms are as defined in the main text.

To obtain the equation of motion for $\pi(\mathbf{K},t)$ we write,

$$\dot{\pi} = \frac{d}{dt}(b_c^* b_v) = \dot{b}_c^* b_v + \dot{b}_v b_c^* \tag{D.3}$$

where for simplicity we have dropped the arguments $(\mathbf{K},t)$. For each of the two terms on the right hand side above we get,

$$\dot{b}_c^* b_v = \Big(- i\Omega b_v^* e^{-iS} \Big) b_v \tag{D.4}$$

$$= -i\Omega n_v e^{-iS} \tag{D.5}$$

and

$$\dot{b}_v b_c^* = \Big(i\Omega b_c e^{-iS} \Big) b_c^* \tag{D.6}$$

$$= i\Omega n_c e^{-iS} \tag{D.7}$$

Now, we do the summation of equations (D.5) and (D.7) and obtain,

$$\dot{\pi} = -i\Omega(n_v - n_c)e^{-iS}. \tag{D.8}$$

Finally, defining $w = n_v - n_c$ and including the phenomenological dephasing term we get,

$$\dot{\pi}(\mathbf{K}, t) = -\frac{\pi(\mathbf{K}, t)}{T_2} - i\Omega(\mathbf{K}, t)w(\mathbf{K}, t)e^{-iS(\mathbf{K},t)}. \tag{D.9}$$

Next we derive the equations for $\dot{n}_c$ and $\dot{n}_v$. To do this we write,

$$\dot{n}_v = \dot{b}_v b_v^* + b_v \dot{b}_v^* \tag{D.10}$$

$$= \Big(i\Omega b_c e^{-iS}\Big)b_v^* + \Big(-i\Omega^* b_c^* e^{iS}\Big)b_v \tag{D.11}$$

which then gives the equation of motion for n_v as,

$$\dot{n}_v(\mathbf{K}, t) = -i\Omega^*(\mathbf{K}, t)\pi(\mathbf{K}, t)e^{iS(\mathbf{K},t)} + \text{c.c.} \tag{D.12}$$

In a similar manner, the equation for $\dot{n}_c$ can be obtained as,

$$\dot{n}_c = \dot{b}_c b_c^* + b_c \dot{b}_c^* \tag{D.13}$$

$$= \Big(i\Omega^* b_v e^{iS}\Big)b_c^* + \Big(-i\Omega b_v^* e^{-iS}\Big)b_c, \tag{D.14}$$

which yields,

$$\dot{n}_c(\mathbf{K}, t) = i\Omega^*(\mathbf{K}, t)\pi(\mathbf{K}, t)e^{iS(\mathbf{K},t)} + \text{c.c.} \tag{D.15}$$

Bibliography

[1] LV Keldysh et al. Ionization in the field of a strong electromagnetic wave. *Sov. Phys. JETP*, 20(5):1307–1314, 1965.

[2] Steeve Augst, Donna Strickland, David D Meyerhofer, See-Leang Chin, and Joseph H Eberly. Tunneling ionization of noble gases in a high-intensity laser field. *Physical review letters*, 63(20):2212, 1989.

[3] Thomas Brabec and Ferenc Krausz. Intense few-cycle laser fields: Frontiers of nonlinear optics. *Reviews of Modern Physics*, 72(2):545, 2000.

[4] Armin Scrinzi, Michael Geissler, and Thomas Brabec. Ionization above the coulomb barrier. *Physical review letters*, 83(4):706, 1999.

[5] Martin Schultze, Krupa Ramasesha, CD Pemmaraju, SA Sato, D Whitmore, A Gandman, James S Prell, LJ Borja, D Prendergast, K Yabana, et al. Attosecond band-gap dynamics in silicon. *Science*, 346(6215):1348–1352, 2014.

[6] Martin Schultze, Elisabeth M Bothschafter, Annkatrin Sommer, Simon Holzner, Wolfgang Schweinberger, Markus Fiess, Michael Hofstetter, Reinhard Kienberger, Vadym Apalkov, Vladislav S Yakovlev, et al. Controlling dielectrics with the electric field of light. *Nature*, 493(7430):75–78, 2013.

[7] Ferenc Krausz and Mark I Stockman. Attosecond metrology: from electron capture to future signal processing. *Nature Photonics*, 8(3):205–213, 2014.

[8] Agustin Schiffrin, Tim Paasch-Colberg, Nicholas Karpowicz, Vadym Apalkov, Daniel Gerster, Sascha Mühlbrandt, Michael Korbman, Joachim Reichert, Martin Schultze, Simon Holzner, et al. Optical-field-induced current in dielectrics. *Nature*, 493(7430):70–74, 2013.

[9] Tran Trung Luu, M Garg, S Yu Kruchinin, Antoine Moulet, M Th Hassan, and Eleftherios Goulielmakis. Extreme ultraviolet high-harmonic spectroscopy of solids. *Nature*, 521(7553):498–502, 2015.

[10] VE Gruzdev. Photoionization rate in wide band-gap crystals. *Physical Review B*, 75(20):205106, 2007.

[11] PA Zhokhov and AM Zheltikov. Field-cycle-resolved photoionization in solids. *Physical review letters*, 113(13):133903, 2014.

[12] Peter G Hawkins and Misha Yu Ivanov. Role of subcycle transition dynamics in high-order-harmonic generation in periodic structures. *Physical Review A*, 87(6):063842, 2013.

[13] Rafael R Gattass and Eric Mazur. Femtosecond laser micromachining in transparent materials. *Nature photonics*, 2(4):219–225, 2008.

[14] Mehmet Fatih Yanik, Hulusi Cinar, Hediye Nese Cinar, Andrew D Chisholm, Yishi Jin, and Adela Ben-Yakar. Neurosurgery: functional regeneration after laser axotomy. *Nature*, 432(7019):822–822, 2004.

[15] Maria Farsari and Boris N Chichkov. Materials processing: Two-photon fabrication. *Nature photonics*, 3(8):450–452, 2009.

[16] Tim D Gerke and Rafael Piestun. Aperiodic volume optics. *Nature photonics*, 4(3):188–193, 2010.

[17] Annkatrin Sommer, EM Bothschafter, SA Sato, Clemens Jakubeit, Tobias Latka, Olga Razskazovskaya, Hanieh Fattahi, Michael Jobst, W Schweinberger, Vage Shirvanyan, et al. Attosecond nonlinear polarization and light–matter energy transfer in solids. *Nature*, 534(7605):86–90, 2016.

[18] Kirill A Pronin, André D Bandrauk, and Alexander A Ovchinnikov. Harmonic generation by a one-dimensional conductor: Exact results. *Physical Review B*, 50(5):3473, 1994.

[19] Shambhu Ghimire, Anthony D DiChiara, Emily Sistrunk, Pierre Agostini, Louis F DiMauro, and David A Reis. Observation of high-order harmonic generation in a bulk crystal. *Nature physics*, 7(2):138–141, 2011.

[20] Michael Krüger, Markus Schenk, and Peter Hommelhoff. Attosecond control of electrons emitted from a nanoscale metal tip. *Nature*, 475(7354):78–81, 2011.

[21] Ben Zaks, Ren-Bao Liu, and Mark S Sherwin. Experimental observation of electron-hole recollisions. *Nature*, 483(7391):580–583, 2012.

[22] Matthias Hohenleutner, Fabian Langer, Olaf Schubert, Matthias Knorr, U Huttner, SW Koch, M Kira, and Rupert Huber. Real-time observation of interfering crystal electrons in high-harmonic generation. *Nature*, 523(7562):572–575, 2015.

[23] G Vampa, TJ Hammond, N Thiré, BE Schmidt, F Légaré, CR McDonald, T Brabec, and PB Corkum. Linking high harmonics from gases and solids. *Nature*, 522(7557):462–464, 2015.

[24] Giulio Vampa, TJ Hammond, Nicolas Thiré, BE Schmidt, François Légaré, CR McDonald, Thomas Brabec, DD Klug, and PB Corkum. All-optical reconstruction of crystal band structure. *Physical review letters*, 115(19):193603, 2015.

[25] Hartmut Haug and Stephan W Koch. Quantum theory of the optical and electronic properties of semiconductors 4^{th} edition, 2004,.

[26] CR McDonald, G Vampa, PB Corkum, and T Brabec. Intense-laser solid state physics: Unraveling the difference between semiconductors and dielectrics. *Physical Review Letters*, 118(17):173601, 2017.

[27] Maciej Lewenstein, Ph Balcou, M Yu Ivanov, Anne Lhuillier, and Paul B Corkum. Theory of high-harmonic generation by low-frequency laser fields. *Physical Review A*, 49(3):2117, 1994.

[28] Robert W Boyd. *Nonlinear optics*. Academic press, 2003.

[29] Charles Kittel. *Introduction to solid state physics*. Wiley, 2005.

[30] Alan Jeffrey and Daniel Zwillinger. *Table of integrals, series, and products*. Academic press, 2007.

[31] Neil W Ashcroft, N David Mermin, and Sergio Rodriguez. Solid state physics, 1998.

[32] David Ronald Kincaid and Elliott Ward Cheney. *Numerical analysis: mathematics of scientific computing*, volume 2. American Mathematical Soc., 2002.

[33] William H Press, Saul A Teukolsky, William T Vetterling, and Brian P Flannery. *Numerical recipes in C*, volume 2. Cambridge university press Cambridge, 1996.